

A Discontinuous-Galerkin-Hancock Method for Viscous CFD and Multiphase Flows using First-Order PDEs

S. Alireza Miri and James G. M^cDonald
Corresponding author: smiri047@uOttawa.ca

Department of Mechanical Engineering, University of Ottawa
161 Louis Pasteur, Ottawa, Ontario, Canada, K1N 6N5

Abstract: This paper investigates the ability for first-order partial differential equations to predict viscous gas-flow and multiphase phenomena. The models used are moment closures from the kinetic theory of gases. The first large-scale implementation of a discontinuous-Galerkin-Hancock method with adaptive mesh refinement is demonstrated. This scheme was developed specifically for the efficient solution of the hyperbolic-relaxation equations that result from moment closures. The first-order nature of the partial differential equations make them relatively insensitive to low quality meshes that often result from adaptive mesh refinement. The optimal locality of the numerical method makes it ideal for the solution of first-order moment methods on large-scale computers. Solutions to several canonical flow problems are demonstrated and show the ability for the moment methods to very efficiently compute predictions for viscous flows.

Keywords: Discontinuous Galerkin Methods, Moment Methods.

1 Introduction

The compressible Navier-Stokes equations have been an immensely successful model for viscous gas-flow prediction. In fact, these equations can usually produce predictions that have such high accuracy that people can be forgiven for forgetting that they are only a model. However, in regimes where length scales of interest begin to approach the mean free path and the continuum assumption is violated, physically inaccurate results are obtained. In addition to the physical limitations of the Navier-Stokes equations, the partial differential equations that describe the model have mathematical properties that can make numerical solution inconvenient. For example, the second-order spacial derivatives present in the partial differential equations (PDEs) can cause solutions to be overly sensitive to grid quality [1].

Moment methods from the kinetic theory of gases exist as an alternative to the Navier-Stokes model. Models in this family are described by first-order hyperbolic PDEs with local relaxation. Rather than including second-derivatives, the moment models include higher-order moments in the solution vector. This provides a natural treatment for non-equilibrium effects and expands the regime for which the model is physically applicable past the Navier-Stokes level. When combined with appropriate numerical techniques, solutions can be reliably and efficiently calculated on distributed-memory computers using meshes that may contain sharp irregularities.

Discontinuous-Galerkin (DG) methods are very well suited for distributed parallel solution of first-order PDEs. This is because the optimal locality of the method minimizes needed communication between computational processes. A highly efficient, coupled space-time DG method that achieves third-order accuracy in both space and time while using only linear elements has been proposed by Suzuki and van Leer [2, 3]. Third-order accuracy is obtained through the use of a technique originally proposed by Hancock [4]. This discontinuous-Galerkin Hancock (DGH) scheme was specifically designed for the solution of PDE resulting from moment closures, however it has not previously been implemented on a large scale. The combination of moment methods with the DGH discretization leads to a very efficient numerical treatment for viscous compressible gas flows that is accurate both in and out of local thermodynamic equilibrium.

In Section 2 of this paper, the background of moment methods are reviewed. Following this, Section 3 introduces the discontinuous-Galerkin-Hancock method. Section 4 explains details of the current distributed adaptive-mesh-refinement implementation. Finally, Section 5 shows numerical results for several canonical flow problems.

2 Moment Methods

Rather than starting from the assumption that the fluid can be treated as a continuum, one can begin from a molecular treatment of a gas. In the kinetic theory of gases, this is done probabilistically. In this theory, gas particles are not treated individually. Rather, a distribution function, \mathcal{F} , is defined that gives the phase-space density of particles at a point in space, x_i , with a particular velocity, v_i at a given time, t . In the absence of external acceleration fields, the evolution of this distribution function is given by the Boltzmann equation,

$$\frac{\partial \mathcal{F}}{\partial t} + v_i \frac{\partial \mathcal{F}}{\partial x_i} = \frac{\delta \mathcal{F}}{\delta t}. \quad (1)$$

This equation appears to be very simple, however it is very high dimensional (three space dimensions, three velocity dimensions, plus time). The numerical expense of a direct discretization is therefore extremely high. Also, the right-hand side is known as the collision operator and models the effects of inter-particle collisions on the distribution. In general it is a complex integral relation in five dimensions and is extremely difficult to evaluate accurately.

Fortunately, the huge amount of information given by \mathcal{F} is rarely needed. Instead, macroscopic “observable” quantities are desired. Traditional variables are related to \mathcal{F} through velocity moments. For example

$$\rho = \iiint_{\infty} m \mathcal{F} dv_i = \langle m \mathcal{F} \rangle, \quad \rho u_i = \langle m v_i \mathcal{F} \rangle, \quad \frac{1}{2} \rho u_i u_i + \frac{p}{\gamma - 1} = \frac{1}{2} \langle m v_i v_i \mathcal{F} \rangle, \quad (2)$$

where m is the mass of a gas particle, ρ is the mass density of the gas, u_i is the macroscopic bulk velocity of the gas, p is the thermodynamic pressure, and $\langle \cdot \rangle$ denotes integration over all possible particle velocities. The bulk velocity can be used to define the random particle velocity as $c_i = v_i - u_i$. This is the difference between a particular particle’s velocity and the local average. Higher-order moments of the distribution function can also be calculated. For example,

$$P_{ij} = \langle m c_i c_j \mathcal{F} \rangle, \quad Q_{ijk} = \langle m c_i c_j c_k \mathcal{F} \rangle. \quad (3)$$

Here, P_{ij} is the pressure tensor. For a monatomic gas, it is related to the traditional thermodynamic pressure as $p = P_{ii}/3$ and to the deviatoric (viscous) stress as

$$\tau_{ij} = \delta_{ij} p - P_{ij}. \quad (4)$$

The third-order tensor, Q_{ijk} , is the generalized heat-flux tensor and is related to the traditional heat-flux vector as

$$q_i = \frac{1}{2} Q_{ijj} = \frac{1}{2} \langle m c_i c_j c_j \mathcal{F} \rangle. \quad (5)$$

Evolution equations for these macroscopic moments can be obtained by taking a chosen set of moments of the Boltzmann equation directly [5]. For example, for an arbitrary velocity weight, w , an evolution equation for the corresponding moment can be found as

$$\frac{\partial}{\partial t} \langle m w \mathcal{F} \rangle + \frac{\partial}{\partial x_i} \langle m w v_i \mathcal{F} \rangle = \Delta(w). \quad (6)$$

Here, $\Delta(w)$ represents the effect of collisions on the moment of interest. Normally, one is interested in the evolution of more than one moment. By generating a collection of equations of the form given in Eq. (6), a

system of PDEs can be obtained that has the form

$$\frac{\partial}{\partial t} \mathbf{U} + \frac{\partial}{\partial x_i} \mathbf{F}_i = \mathbf{S}. \quad (7)$$

Here, \mathbf{U} , is a solution vector containing an expanded number of velocity moments as compared to traditional methods, \mathbf{F}_i is the flux dyad, and \mathbf{S} is a local algebraic source term that can be quite stiff for dense-gas situations.

The first-order balance-law form of Eq. (7) is very appealing. Unfortunately, things are not so simple. In general, the flux dyad and source vector are not known functions of the solution vector. The system is not closed.

Fortunately, for many practical situations, simplified collision operators can be used. These allow the right-hand side of Eq. (7) to be determined as a function of the solution vector, \mathbf{U} . The flux dyad, however, is more difficult. As can be observed from Eq (6), the flux will always contain moments that are one order higher in terms of velocity than the entry in \mathbf{U} .

In order to close the system, usually restrictions are placed on the form of allowable distribution functions, \mathcal{F} . This assumed form of \mathcal{F} is chosen such that it contains the same number of free parameters and there are moments in \mathbf{U} . The value of these parameters is set such that the moment relations, such as those shown in Eqs. (2) and (3) are satisfied. Any moment needed for the flux dyad can then simply be integrated, as the assumed expression for \mathcal{F} is then known. This technique is known as a moment closure.

The original moment-closure technique is due to Grad [5]. In this method, the distribution function is expanded around the local equilibrium distribution in terms of polynomials of the particle velocity. Though this leads to a closed model, the resulting equations can become ill-posed. This is caused by the fact that the eigenvalues of the resulting flux Jacobian can become complex.

More recently, a much more elegant choice for \mathcal{F} has been proposed [6, 7, 8]. In this technique, the distribution function is assumed to have the form that is consistent with the moments present in \mathbf{U} , while maximizing entropy. The resulting form of \mathcal{F} is

$$\mathcal{F} = e^{p(v_i)}, \quad (8)$$

where $p(v_i)$ is a polynomial of the particle velocity. In contrast to the Grad method, this assumed form is guaranteed to be positive and can be shown to lead to hyperbolic PDEs whenever a distribution function of the form given in Eq (8) can be found that correspond to the moments in \mathbf{U} . Unfortunately, for high-order moment methods, there are valid physical gas states for which a corresponding distribution function of this form does not exist [9]. Initially this seemed to be a devastating blow to the maximum-entropy idea, however more recent work has shown that these areas of non-definition can be handled in practice [10, 11]. In any event, the questions of existence of high-order moment closures is not the subject of the current work. All models used in the present study are of low enough order that well-posedness is guaranteed.

Moment models, derived through the maximum-entropy theory, bring many advantages as compared to the traditional Navier-Stokes equations. Firstly, the fact that they are derived from a more fundamental physical description of a gas means that they can produce physically accurate solutions in situations when the Navier-Stokes equations are an incorrect model [1, 11]. Typically, the solution vector in moment methods contain ten or more unknowns. These include the classical mass, momentum, and energy density, but also extra degrees of freedom for higher-order statistics of gas particle velocities. This brings added modelling fidelity in extreme situations and allows the model to maintain physical accuracy well out of the traditional continuum regime.

In addition to physical advantages, moment methods bring many numerical advantages as compared to the Navier-Stokes equations. The fact that all derivatives are first order means that an extra order of spacial accuracy is often possible for a given stencil or polynomial representation of the approximate solution. For explicit methods, the time-step restriction is proportional to Δx , rather than Δx^2 , which can lead to more efficient time integration. Also, it has been demonstrated that the first-order nature of moment methods make them far less sensitive to grid irregularities [1]. Lower-quality grids are often unavoidable for practical situation or when adaptive mesh refinement (AMR) is used. The use of models that maintain high-quality solutions on low quality meshes is very desirable.

2.1 Multiphase Flow

Moment methods are not only applicable to perfect gases. The situation of a large number of particles or micro-droplets in a multiphase flow is very similar to the situation of many particles making up a gas. It is therefore expected that the moment technique can also be used to derive advanced models for disperse multiphase flows. In fact, recent work in this field has begun to yield very promising results [12, 13].

One physical process in the field of multiphase flow that has traditionally been difficult for Eulerian field-based methods to predict is the crossing of streams of non-interacting particles. In order to demonstrate this modelling artifact, Vié *et al.* constructed a difficult test case involving two beams of particles in a compressive acceleration field that cross numerous times [12]. The exact solution to their problem is shown graphically in Figure 1(a). Two streams of particles enter on the left and are accelerated towards the centre. As the streams move to the right, they cross several times. This case is designed such that the particle density is infinite at the crossing points.

One very widely used Eulerian model for multiphase flow is described by two equations,

$$\frac{\partial}{\partial t} \rho + \frac{\partial}{\partial x_i} (\rho u_i) = 0, \quad (9)$$

$$\frac{\partial}{\partial t} (\rho u_j) + \frac{\partial}{\partial x_i} (\rho u_i u_j) = \frac{\rho}{\tau} (V_j - u_j). \quad (10)$$

Here, V_j is the velocity of the background flow and τ is a relaxation time for particle acceleration due to the drag force. Though not usually thought of in this way, this commonly used model is actually a moment method. It results from assuming that the distribution function describing particle velocities is described by a delta, as

$$\mathcal{F} = \rho \delta(v_i - u_i). \quad (11)$$

That is, all particles at a location in space and time are assumed to have the same velocity. When this model is used to predict the solution to the crossing-beam problem, the result shown in Figure 1(b). One can see that the beams are completely incapable of crossing. This is a direct result of the assumed form of \mathcal{F} , which does not allow particles to have multiple velocities at the crossing point.

Recently, Forgues and M^cDonald have developed a fourteen-moment model for monodisperse particle flow prediction based on the maximum-entropy theory [13]. They have demonstrated that their first-order hyperbolic Eulerian model does allow particle beams to cross. Numerical solution of the crossing-beam problem using their method is shown in Figure 1(c). Clearly this result is immensely more satisfying than the that obtained with the traditional method.

3 The Discontinuous-Galerkin-Hancock Method

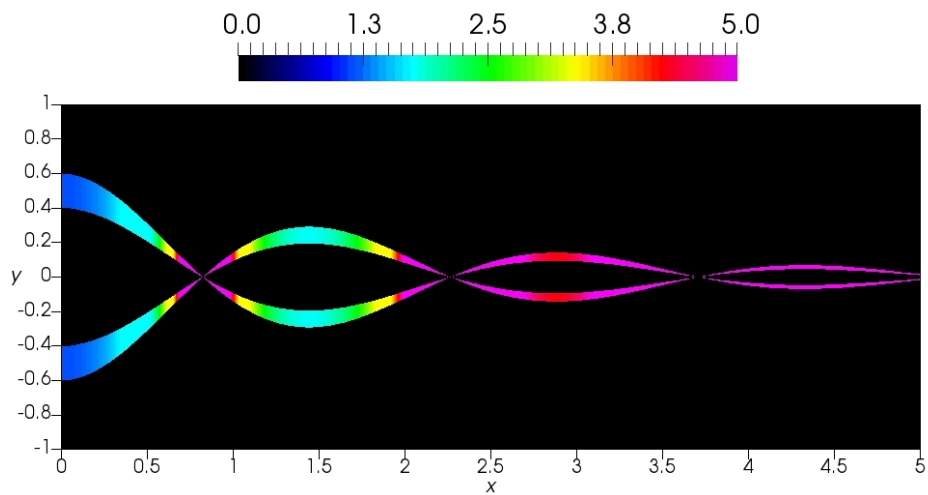
Moment methods hold the promise of new models for gas and multiphase flow that possess many physical and mathematical advantages over traditional methods. Their first-order nature make them well suited for solution on parallel computers. Particularly, discontinuous-Galerkin-style methods seem good candidates for their numerical solution.

The numerical method presented in this work is a two-dimensional finite-element scheme that was originally proposed by Suzuki and van Leer [2, 3]. It was created specifically to allow for the efficient solutions of hyperbolic PDEs that result from moment methods. Important aspects of the scheme are summarized here. The interested reader should consult Suzuki [3] for a detailed explanation of all aspects of the technique.

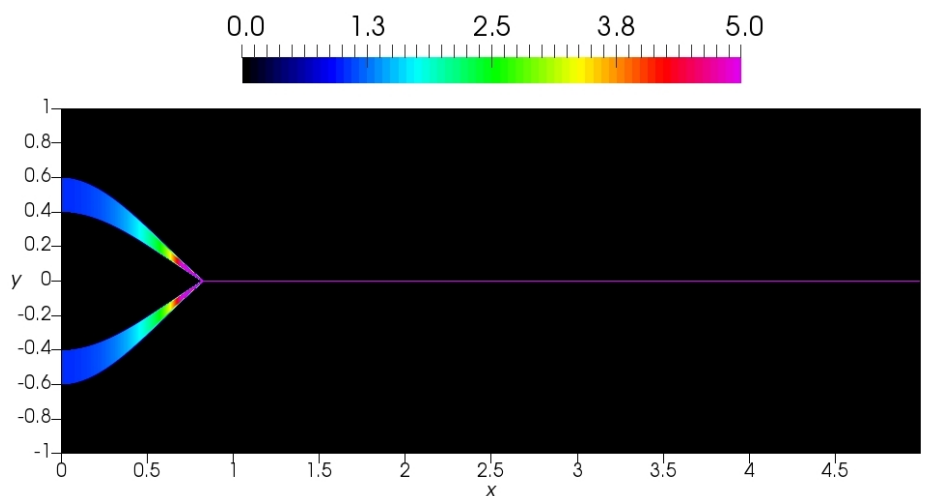
Galerkin methods are highly successful finite-element methods. The DGH method used here is a coupled space-time method. That is to say, weak solutions of the governing PDEs are sought such that the product of the PDE with a test function, integrated through space and time, should be satisfied,

$$\iint_{\Omega \times T} \nu \frac{\partial}{\partial t} \mathbf{U} \, dx_j \, dt = - \iint_{\Omega \times T} \nu \frac{\partial}{\partial x_i} \mathbf{F}_i \, dx_j \, dt + \iint_{\Omega \times T} \nu \mathbf{S} \, dx_j \, dt. \quad (12)$$

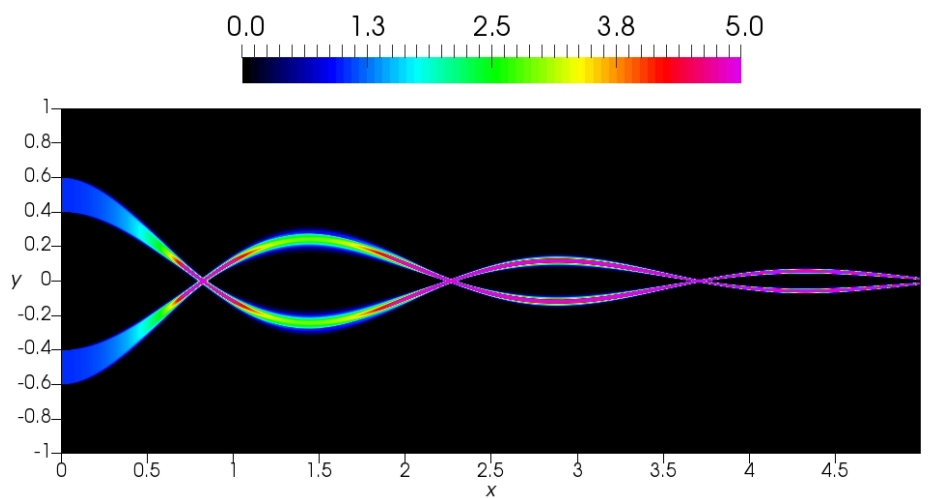
Here, $\Omega \times T$ is the domain made up of the space of the problem and the time interval from time step n to $n + 1$, while ν is an arbitrary test function. In order to obtain a practical numerical method, a finite number



(a) *Exact solution*



(b) *Traditional Eulerian method*



(c) *Fourteen-moment method*

Figure 1: *Particle density for two rightward-moving beams of non-interacting particles in a compressive acceleration field.*

of test functions, ν , are selected. For the present method, three test functions are chosen for each cell in a computational mesh. These test functions are only non-zero within one cell, in which they have the form

$$\nu_1 = 1, \quad \nu_2 = x - \tilde{x}_\kappa, \quad \nu_3 = y - \tilde{y}_\kappa,$$

where (\tilde{x}, \tilde{y}) are the coordinates of the area centroid of the cell of interest (cell κ).

As each test function is only non-zero in one cell, the spacial domain of integration in Eq (12) can be reduced to that of one cell, Ω_k . Integration by parts is then used to remove derivatives from the solution and its flux,

$$\int_T \nu \frac{\partial}{\partial t} \mathbf{U} dt = (\mathbf{U}^{n+1} \nu - \mathbf{U}^n \nu) - \int_T \mathbf{U} \frac{\partial \nu}{\partial t} dt, \quad (13)$$

$$\int_{\Omega_k} \nu \frac{\partial}{\partial x_i} \mathbf{F}_i dx_j = \int_{\Gamma_k} \nu \mathbf{F}_i \hat{n}_i d\Gamma - \int_{\Omega_k} \mathbf{F}_i \frac{\partial \nu}{\partial x_i} dx_j. \quad (14)$$

Here, Γ is the boundary of the two-dimensional cell.

As the test functions are constant in time, by substituting Eq. (13) and Eq. (14) into Eq. (12), the formulation simplifies to

$$\int_{\Omega_k} \nu (\mathbf{U}^{n+1} - \mathbf{U}^n) dx_j = - \iint_{\Gamma_k \times T} \nu \mathbf{F}_i \hat{n}_i d\Gamma dt + \iint_{\Omega_k \times T} \mathbf{F}_i \frac{\partial \nu}{\partial x_i} dx_j dt + \iint_{\Omega_k \times T} \nu \mathbf{S} dx_j dt. \quad (15)$$

The numerical solution variables are taken to be the cell average value, $\overline{\mathbf{U}}$, and average value of the x and y components of the solution gradient within each cell ($\overline{\partial_x \mathbf{U}}$ and $\overline{\partial_y \mathbf{U}}$). The assumed solution in the k^{th} cell is therefore

$$\mathbf{U}_\kappa = \overline{\mathbf{U}}_\kappa + (\overline{\partial_x \mathbf{U}})_\kappa (x - \tilde{x}_\kappa) + (\overline{\partial_y \mathbf{U}})_\kappa (y - \tilde{y}_\kappa). \quad (16)$$

Insertion of the assumed form of the solution into Eq. (15) and integration with each test function yields update formulas for the degrees of freedom as

$$\overline{\mathbf{U}}_\kappa^{n+1} = \overline{\mathbf{U}}_\kappa^n + \frac{1}{A_\kappa} \left(- \iint_{\partial \Gamma_\kappa \times T} \mathbf{F}_i \hat{n}_i d\Gamma dt + \iint_{\Omega_\kappa \times T} \mathbf{S} dx_j dt \right), \quad (17)$$

and

$$\begin{aligned} \begin{bmatrix} \overline{\partial_x \mathbf{U}}_\kappa^{n+1} \\ \overline{\partial_y \mathbf{U}}_\kappa^{n+1} \end{bmatrix} &= \begin{bmatrix} \overline{\partial_x \mathbf{U}}_\kappa^n \\ \overline{\partial_y \mathbf{U}}_\kappa^n \end{bmatrix} + \overline{\mathbf{K}}_\kappa \left(- \iint_{\partial \Gamma_\kappa \times T} \begin{bmatrix} x - \tilde{x}_\kappa \\ y - \tilde{y}_\kappa \end{bmatrix} \mathbf{F}_i \hat{n}_i d\Gamma dt \right. \\ &\quad \left. + \iint_{\Omega_\kappa \times T} \begin{bmatrix} \mathbf{F}_x \\ \mathbf{F}_y \end{bmatrix} dx_j dt + \iint_{\Omega_\kappa \times T} \begin{bmatrix} x - \tilde{x}_\kappa \\ y - \tilde{y}_\kappa \end{bmatrix} \mathbf{S} dx_j dt \right). \end{aligned} \quad (18)$$

Here, A_κ is the area of cell κ and $\overline{\mathbf{K}}_\kappa$ is the matrix given by

$$\overline{\mathbf{K}}_\kappa = \begin{bmatrix} K_{xx} & K_{xy} \\ K_{xy} & K_{yy} \end{bmatrix}^{-1}, \quad (19)$$

with

$$K_{xx} = \iint_{\Omega_\kappa} (x - \tilde{x}_\kappa)^2 dx_j, \quad K_{xy} = \iint_{\Omega_\kappa} (x - \tilde{x}_\kappa)(y - \tilde{y}_\kappa) dx_j, \quad K_{yy} = \iint_{\Omega_\kappa} (y - \tilde{y}_\kappa)^2 dx_j \quad (20)$$

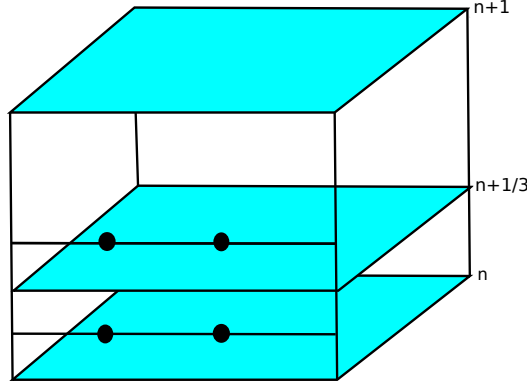


Figure 2: *Quadrature points for surface flux integration on a space-time element, blue slices represent instances in time when solution data is known or computed*

begin the area moments of inertia of the cell.

3.1 Cell-Average Update

For many applications, the PDEs resulting from moment methods contain very stiff local source terms. To alleviate this problem, it is desirable to treat the source term implicitly. This does not generally add an excessive numerical expense, as the source terms are local and do not couple between cells. For the present method, Suzuki chose to use the Radau IIA method for the source-term time integration [3]. This method requires that an intermediate solution state be added at time level $n + \frac{1}{3}$.

The surface flux integrals in Eq. (17) is evaluated using the midpoint rule in the time dimension and two-point Gaussian quadrature on each edge of the cell for the space dimension. As the solution is discontinuous along the edge, a numerical flux function must be used. In the present work, the HLLE flux function is used [14, 15]. As the Radau II method requires the solution at an intermediate $n + \frac{1}{3}$ step be calculated, four quadrature points per edge are needed. The quadrature points used for inter-cellular flux calculations are shown graphically in Figure 2. For this quadrature rule, the solution at the half-time for each update is needed as inputs to the flux functions. Predicting values at these points is Hancock's contribution to the method [4].

The solution state that is used for the input to inter-cell flux calculations is predicted using data that is internal to the cell. For this, the sub-cell solution is approximated as

$$\begin{aligned} \tilde{\mathbf{U}}_{\kappa}^{n+\psi}(x, y) = & \bar{\mathbf{U}}_{\kappa}^n + \phi_{\kappa} \wedge (\bar{\partial}_x \bar{\mathbf{U}}_{\kappa}^n)(x - \tilde{x}_{\kappa}) + \phi_{\kappa} \wedge (\bar{\partial}_y \bar{\mathbf{U}}_{\kappa}^n)(y - \tilde{x}_{\kappa}) \\ & - \frac{\psi \Delta t}{A_{\kappa}} \int_{\partial \Gamma_{\kappa}} \mathbf{F}_i(\tilde{\mathbf{U}}_{\kappa}^n) \hat{n}_i d\Gamma + \psi \Delta t \mathbf{S}(\tilde{\mathbf{U}}_{\kappa}^{n+\psi}(x, y)). \end{aligned} \quad (21)$$

Here, ϕ is a vector of slope limiters that may be used to ensure stability of discontinuous solutions, \wedge denotes a term-wise product, and Ψ will be either a half or a sixth. The path integral is evaluated using the solution state within the cell and the jump at the cell boundary is not considered. As the source term is treated implicitly, this can lead to a nonlinear system of equations. Suzuki advocates using Newton's method, however, for the present work, the linearization

$$\mathbf{S}(\tilde{\mathbf{U}}_{\kappa}^{n+\psi}(x, y)) = \mathbf{S}(\tilde{\mathbf{U}}_{\kappa}^n(x, y)) + \frac{\partial \mathbf{S}^n}{\partial \mathbf{U}} \left(\tilde{\mathbf{U}}_{\kappa}^{n+\psi}(x, y) - \tilde{\mathbf{U}}_{\kappa}^n(x, y) \right) \quad (22)$$

is used. This leads to a linear system that can be solved efficiently.

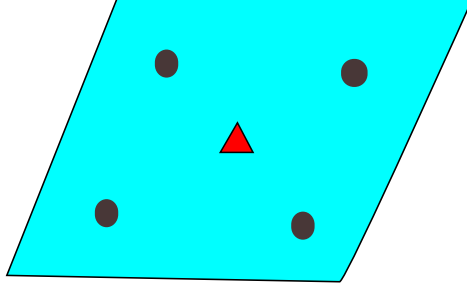


Figure 3: Quadrature points for volume flux integral (\bullet) and source integral (Δ) on a space element.

The final update formula for the cell-average values is

$$\begin{bmatrix} \bar{\mathbf{U}}_{\kappa}^{n+\frac{1}{3}} \\ \bar{\mathbf{U}}_{\kappa}^{n+1} \end{bmatrix} = \begin{bmatrix} \bar{\mathbf{U}}_{\kappa}^n \\ \bar{\mathbf{U}}_{\kappa}^n \end{bmatrix} - \frac{\Delta t}{A_{\kappa}} \begin{bmatrix} \frac{1}{3} \sum_{\zeta} w_{\zeta} \tilde{\mathbf{F}}_{\zeta}^{n+\frac{1}{6}} \\ \sum_{\zeta} w_{\zeta} \tilde{\mathbf{F}}_{\zeta}^{n+\frac{1}{2}} \end{bmatrix} + \Delta t \begin{bmatrix} \frac{5}{12} \mathbf{I} & -\frac{1}{12} \mathbf{I} \\ \frac{3}{4} \mathbf{I} & \frac{1}{4} \mathbf{I} \end{bmatrix} \begin{bmatrix} \bar{\mathbf{S}}^{n+\frac{1}{3}} \\ \bar{\mathbf{S}}^{n+1} \end{bmatrix}. \quad (23)$$

Here, the path integrals around the cell boundary have been replaced by quadrature rules with weights, w_{ζ} . These weights include the edge length. The inter-cell flux function, $\tilde{\mathbf{F}}$ is evaluated using Eq. (21) to produce the inputs on either side of the edge. The source term is evaluated at the cell centre. It is again linearized as

$$\bar{\mathbf{S}}_{\kappa}^{n+\Psi} = \bar{\mathbf{S}}_{\kappa}^n + \left(\frac{\partial \bar{\mathbf{S}}}{\partial \bar{\mathbf{U}}} \right)_{\kappa}^n \left(\bar{\mathbf{U}}_{\kappa}^{n+\Psi} - \bar{\mathbf{U}}_{\kappa}^n \right). \quad (24)$$

3.2 Slope Update

Once the cell average values at time intervals $n + \frac{1}{3}$ and $n + 1$ are known, the updates for the slopes can be computed. The previously computed inter-cell fluxes are used again in the surface flux integral from Eq. (18). The volume-flux integral is evaluated using two-dimensional, four-point Gaussian quadrature based on an assumed solution where the cell-average has been updated, but slopes at time level n are used. Quadrature locations for the slope update are shown in Figure 3.

The final update formula for the slopes takes the form

$$\begin{bmatrix} \overline{\partial_x \mathbf{U}}_{\kappa}^{n+\frac{1}{3}} \\ \overline{\partial_y \mathbf{U}}_{\kappa}^{n+\frac{1}{3}} \\ \overline{\partial_x \mathbf{U}}_{\kappa}^{n+1} \\ \overline{\partial_y \mathbf{U}}_{\kappa}^{n+1} \end{bmatrix} = \begin{bmatrix} \overline{\partial_x \mathbf{U}}_{\kappa}^n \\ \overline{\partial_y \mathbf{U}}_{\kappa}^n \\ \overline{\partial_x \mathbf{U}}_{\kappa}^n \\ \overline{\partial_y \mathbf{U}}_{\kappa}^n \end{bmatrix} + \Delta t \mathbf{Y} \begin{bmatrix} \frac{1}{3} \sum_{\zeta} w_{\zeta} (x_{\zeta} - \tilde{x}_{\kappa}) \tilde{\mathbf{F}}_{\zeta}^{n+\frac{1}{6}} \\ \frac{1}{3} \sum_{\zeta} w_{\zeta} (y_{\zeta} - \tilde{y}_{\kappa}) \tilde{\mathbf{F}}_{\zeta}^{n+\frac{1}{6}} \\ \sum_{\zeta} w_{\zeta} (x_{\zeta} - \tilde{x}_{\kappa}) \tilde{\mathbf{F}}_{\zeta}^{n+\frac{1}{2}} \\ \sum_{\zeta} w_{\zeta} (y_{\zeta} - \tilde{y}_{\kappa}) \tilde{\mathbf{F}}_{\zeta}^{n+\frac{1}{2}} \end{bmatrix} + \Delta t \mathbf{Y} \begin{bmatrix} \frac{1}{3} \sum_{\eta} w_{\eta} \left(\frac{1}{2} (\mathbf{F}_x)_{\eta}^n + \frac{1}{2} (\mathbf{F}_x)_{\eta}^{n+\frac{1}{3}} \right) \\ \frac{1}{3} \sum_{\eta} w_{\eta} \left(\frac{1}{2} (\mathbf{F}_y)_{\eta}^n + \frac{1}{2} (\mathbf{F}_y)_{\eta}^{n+\frac{1}{3}} \right) \\ \sum_{\eta} w_{\eta} \left(\frac{3}{4} (\mathbf{F}_x)_{\eta}^{n+\frac{1}{3}} + \frac{1}{4} (\mathbf{F}_x)_{\eta}^{n+1} \right) \\ \sum_{\eta} w_{\eta} \left(\frac{3}{4} (\mathbf{F}_y)_{\eta}^{n+\frac{1}{3}} + \frac{1}{4} (\mathbf{F}_y)_{\eta}^{n+1} \right) \end{bmatrix} + \Delta t \begin{bmatrix} \frac{5}{12} \mathbf{I} & -\frac{1}{12} \mathbf{I} \\ \frac{3}{4} \mathbf{I} & \frac{1}{4} \mathbf{I} \end{bmatrix} \begin{bmatrix} \left(\frac{\partial \bar{\mathbf{S}}}{\partial \bar{\mathbf{U}}} \right)_{\kappa}^{n+\frac{1}{3}} \left(\overline{\partial_x \mathbf{U}}_{\kappa}^{n+\frac{1}{3}} \right) \\ \left(\frac{\partial \bar{\mathbf{S}}}{\partial \bar{\mathbf{U}}} \right)_{\kappa}^{n+\frac{1}{3}} \left(\overline{\partial_y \mathbf{U}}_{\kappa}^{n+\frac{1}{3}} \right) \\ \left(\frac{\partial \bar{\mathbf{S}}}{\partial \bar{\mathbf{U}}} \right)_{\kappa}^{n+1} \left(\overline{\partial_x \mathbf{U}}_{\kappa}^{n+1} \right) \\ \left(\frac{\partial \bar{\mathbf{S}}}{\partial \bar{\mathbf{U}}} \right)_{\kappa}^{n+1} \left(\overline{\partial_y \mathbf{U}}_{\kappa}^{n+1} \right) \end{bmatrix} \quad (25)$$

Here, η is the index through the four-point flux-volume quadrature with w_η as the corresponding weight, \mathbf{I} is the identity matrix and $\mathbf{\Upsilon}$ is the matrix given by

$$\mathbf{\Upsilon} = \begin{bmatrix} \overline{\mathbf{K}}_\kappa & 0 \\ 0 & \overline{\mathbf{K}}_\kappa \end{bmatrix}. \quad (26)$$

Though only linear basis functions are used, this scheme results in third-order accuracy in both space and time, the update in each cell requires neighbouring information only once. It can therefore be said to be optimally efficient for parallel computation as only one message needs to be sent between any two processes during a time step.

4 Adaptive Mesh Refinement

The discontinuous-Galerkin-Hancock method is implemented within a large-scale framework for the parallel solution of hyperbolic-relaxation PDEs. The scheme uses block-based solution-directed adaptive mesh refinement on a body-fitted grid in a manner very similar to Sachdev *et al.* [16] and Gao and Groth [17]. Each block is a quadrilateral structured mesh and all blocks contain the same number of cells. If a particular block is flagged for refinement, it is subdivided into four child blocks, each with the same number of cells as the parent. Efficient load balancing for parallel calculations is achieved simply by dividing the blocks among available processors. Communication between neighbouring blocks is coordinated such that any two CPUs exchange at most one message per time step. Boundary communication between blocks is organized in such a way that blocks of any level of refinement can neighbour each other. That is to say, a cell on the edge of one block can have any number of neighbours. This allows for very flexible and localized mesh refinement.

5 Results

Four cases are considered here. First, a linear hyperbolic-relaxation equation is used to verify the order of accuracy of the scheme. Next a supersonic compressible Euler case is used to demonstrate the mesh refinement as well as the scheme's ability to capture sharp discontinuities. Third, a moment-closure is used to compute a viscous mixing layer. This serves to demonstrate the ability of the first-order PDEs and the DG scheme to efficiently compute viscous solutions. Finally, a moment-closure is used to compute the solution for Stokes flow past a circular cylinder. This case reinforces the hyperbolic PDEs ability to accurately predict viscous phenomena. As this case is very low speed, it also demonstrates the numerical technique's ability to accurately solve problems that are ill-conditioned due to the extremely low Mach number.

5.1 Linear Convection-Relaxation

As a demonstration of the scheme's order of accuracy, a simple convection-relaxation equation is first solved,

$$\frac{\partial \rho}{\partial t} + v_i \frac{\partial \rho}{\partial x_i} = -\frac{1}{\tau} \rho. \quad (27)$$

Here, the convection velocity, v_i , is -1 m/s in both the x and y directions, while the relaxation time is $\tau = 1$ s. The domain is a square with $-10 \text{ m} < x < 10 \text{ m}$ and $-10 \text{ m} < y < 10 \text{ m}$. The initial condition is given by

$$\rho_0 = e^{-\frac{x^2+y^2}{2}}. \quad (28)$$

The exact solution for this situation is

$$\rho_t = e^{-\frac{t}{\tau}} e^{-\frac{(x-v_x t)^2 + (y-v_y t)^2}{2}}. \quad (29)$$

A zero gradient boundary condition is used. Solutions are advanced to a final time of 3s using a CFL number of 0.3, then the ℓ^2 norm of the error is computed. No slope-limiter is used in this case. Table 1 demonstrates the convergence properties of the scheme for a range of resolutions. Clearly, the scheme is

Table 1: Errors: convection-relaxation equation

Number of Cells	ℓ^2 error	Order
50×50	1.2425×10^{-3}	—
100×100	1.8389×10^{-4}	2.76
200×200	2.4139×10^{-5}	2.93
400×400	3.0597×10^{-6}	2.98
800×800	3.8403×10^{-7}	2.99

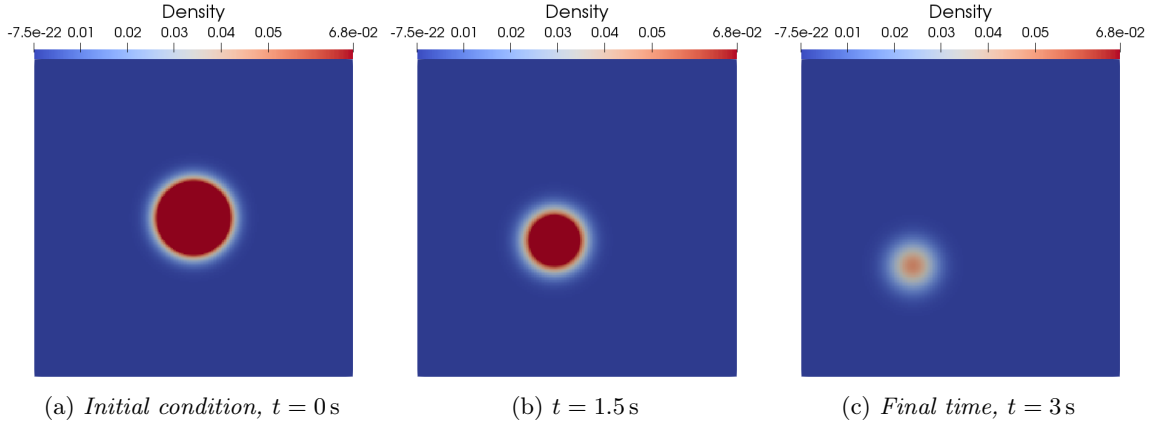


Figure 4: Solutions computed for the convection-relaxation problem computed using a 200×200 mesh.

approaching third-order accuracy as the grid is refined. Figure 4 shows example solutions for this problem computed at three times on a 200×200 mesh.

5.2 Supersonic Inviscid Flow

The next case considered is that of a supersonic inviscid flow through a channel with a bump. The channel is 1 m tall and 5 m long (from $x = -1$ m to 4 m). From $x = 0$ m to $x = 1$ m, a section of a circular arc extends 10% into the channel. The top and bottom boundaries are reflections. The right boundary is a zero-gradient condition, while the left boundary is held fixed. A graphic of the problem is shown in Figure 5.

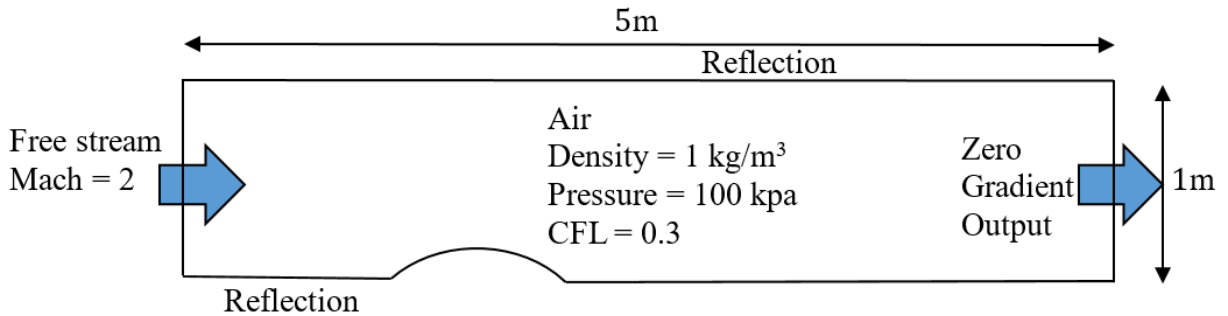


Figure 5: *Bump-channel flow problem.*

The compressible Euler equations are used for this calculation,

$$\frac{\partial \rho}{\partial t} + \frac{\partial}{\partial x_k} (\rho u_k) = 0, \quad (30)$$

$$\frac{\partial}{\partial t} (\rho u_i) + \frac{\partial}{\partial x_k} (\rho u_i u_k + \delta_{ij} p) = 0, \quad (31)$$

$$\frac{\partial}{\partial t} \left(\frac{\rho u_i u_i}{2} + \frac{p}{\gamma - 1} \right) + \frac{\partial}{\partial x_k} \left(u_k \left(\frac{\rho u_i u_i}{2} + \frac{\gamma p}{\gamma - 1} \right) \right) = 0. \quad (32)$$

The Euler equations are the lowest-order member of the maximum-entropy moment hierarchy. They describe a gas that is everywhere in local thermodynamic equilibrium, which is the maximum entropy state subject to constraints on the local mass, momentum, and energy densities.

The gas used in this problem is air with $\rho = 1 \text{ kg/m}^3$, $p = 100 \text{ kPa}$, $\gamma = 1.4$, and a Mach number of 2. For this case, the Venkatakrisnan slope limiter is used to stabilize the discontinuous solution [18]. Again, a CFL number of 0.3 is used.

For this case, the solution is first computed on a mesh of five blocks, each with 6×6 cells. Once steady state is achieved, the mesh is refined and a new steady state is computed. This is repeated four times. The criterion used to flag blocks for refinement is the divergence of the velocity field. This is chosen as it is a good detector of shock waves. Figure 6 shows the series of solutions that are obtained. Clearly, the initial mesh of 180 cells does a poor job of capturing the details of the solution. However, as the mesh is successively refined, the discontinuities are efficiently captured. The final mesh, after four rounds of mesh refinement, has 572 blocks and 20 592 cells. If the entire mesh was at the same resolution as the most-refined blocks of this mesh, it would contain more than double the number of cells used here.

The flexibility of the connectivity of the blocks is also clear to see in Figure 6. For example, the left-most block is upstream of the initial shock and therefore contains a constant solution state. It is therefore never flagged for refinement. It is neighbored on the right by nine different blocks at three different refinement levels. Smaller blocks can also straddle the cell boundaries of the larger block.

It should be noted that the choice of refinement criterion for this study is somewhat arbitrary. Surely the overall accuracy of the solution is not maximized by this choice. However, the goal is simply to demonstrate the flexibility of the mesh refinement technique and the robustness of the numerics to highly discontinuous solutions and mesh resolutions.

5.3 Viscous Mixing Layer

This case is a low-speed viscous mixing layer. This situation demonstrates the ability for a first-order moment method to accurately capture a classical viscous result. For this demonstration, the Gaussian ten-moment model is used. This moment closure has ten equations that predict the evolution of mass, momentum, and the anisotropic pressure tensor, P_{ij} , which is related to the fluid stresses by Eq. (4). The PDEs that describe the model can be written as

$$\frac{\partial \rho}{\partial t} + \frac{\partial}{\partial x_k} (\rho u_k) = 0, \quad (33)$$

$$\frac{\partial}{\partial t} (\rho u_i) + \frac{\partial}{\partial x_k} (\rho u_i u_k + P_{ik}) = 0, \quad (34)$$

$$\frac{\partial}{\partial t} (\rho u_i u_j + P_{ij}) + \frac{\partial}{\partial x_k} (\rho u_i u_j u_k + u_i P_{jk} + u_j P_{ik} + u_k P_{ij}) = -\frac{1}{3\tau} (3P_{ij} - \delta_{ij} P_{kk}).$$

Here, the collision integral on the right-hand side has been replaced by the BGK collision operator [19]. This simplified operator allows non-equilibrium effects to relax away on a timescale τ . The relaxation time can be chosen such that, in the continuum regime, the model recovers the viscosity of a Newtonian gas, μ . This is done by defining $\mu = \tau p$.

The particular mixing layer studied here is made up of two layers of Argon with standard atmospheric temperature and pressure. The viscosity of Argon is taken as $\mu = 2.117 \times 10^{-5} \text{ Pa}\cdot\text{s}$. Initially, the line $y = 0 \text{ m}$ separates a stream flowing rightward at $\hat{u} = 1 \text{ m/s}$ from a stream flowing leftward at the same

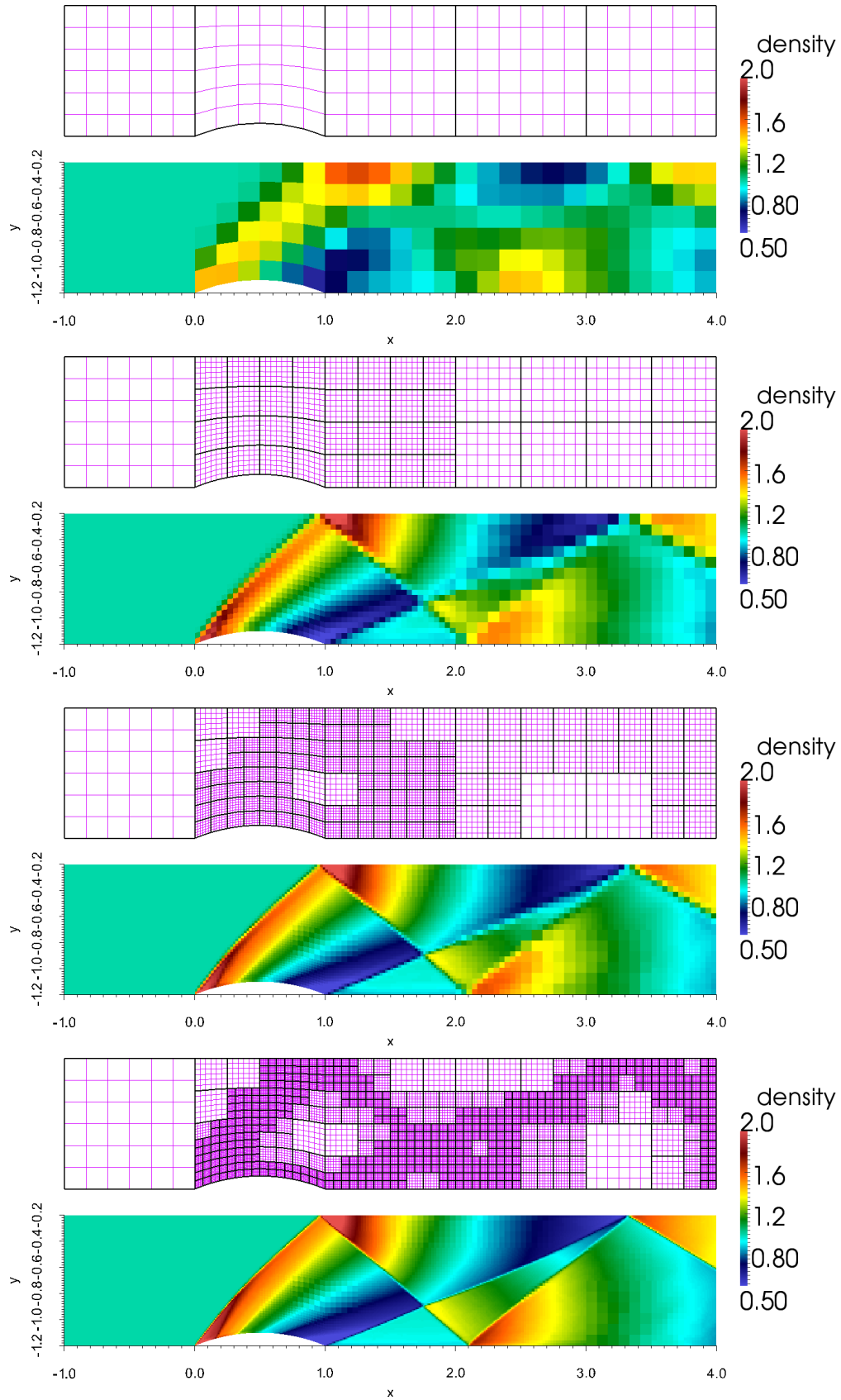


Figure 6: *Bump-channel flow with a Mach number of 2 computed using the compressible Euler equations using zero, two, three, and four levels of mesh refinement.*

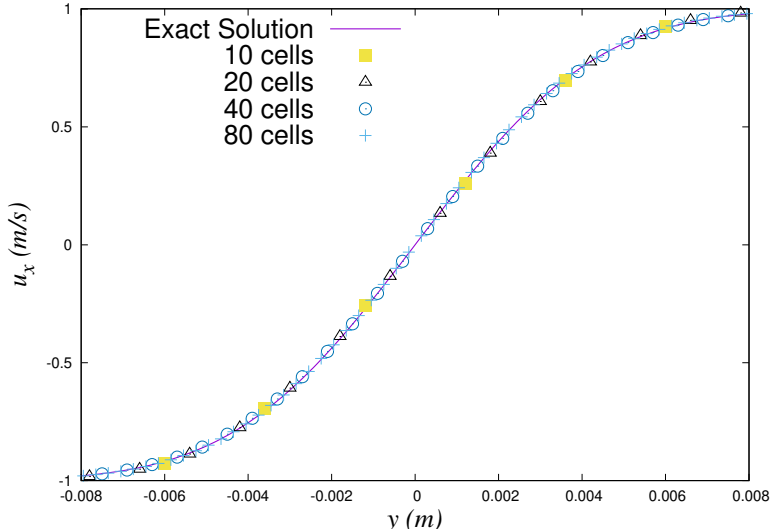


Figure 7: *Mixing-layer prediction using the Gaussian 10-moment closure as compared to the exact solution for incompressible Navier-Stokes.*

speed. The traditional incompressible Navier-Stokes solution for this situation can be computed analytically and is given by

$$u_x = \hat{u} \operatorname{erf} \left(\frac{y}{2} \sqrt{\frac{\rho}{\mu t}} \right). \quad (35)$$

The goal is to recover this same solution using the numerical scheme applied to the Gaussian equations.

For this calculation, the domain in the y direction is taken to be $-0.012 \text{ m} < y < 0.012 \text{ m}$. As this is a one-dimensional calculation, only two cells are used in the x direction along with periodic boundary conditions. A zero-gradient boundary condition is used in the y direction. The Venkatakrishnan slope limiter is again used along with a CFL number of 0.4. The final time of the calculation is $t = 0.5 \text{ s}$.

A zoom-in on results in the area around the mixing layer are shown in Figure 7. Solutions are computed using 10, 20, 40, and 80 cells in the y direction. As can clearly be seen, in all cases the solution of the first-order hyperbolic PDEs agree extremely well with the traditional Navier-Stokes solution. It seems that having a half-dozen cells in the mixing layer is all that is necessary to have near perfect agreement.

The low errors observed in this study are especially impressive given the very low speed of the flow. The Mach number of this flow is less than 0.01, yet the excessive diffusion that would normally result from a compressible solver is not apparent. This is not a result of the use of a moment-method, but rather a result of the extremely low dissipation of the discontinuous-Galerkin-Hancock scheme.

5.4 Stokes Flow Over Cylinder

The final case that demonstrated in this paper is low-Reynolds-number Stokes flow past a circular cylinder. The goal of this case is to again demonstrate the ability of the first-order method to accurately capture a classical viscous result. The fluid is Argon with a density of $\rho = 1.784 \text{ kg/m}^3$, free-stream velocity and pressure of 0.5 m/s and 101325 Pa , and viscosity of $\mu = 2.117 \times 10^{-5} \text{ Pa}\cdot\text{s}$. The cylinder diameter is $1 \times 10^{-5} \text{ m}$. This corresponds to a Reynolds number of 0.421 and Knudsen number of 0.0063. The Mach number in this case is 0.0018. A schematic of this problem is shown in Figure 8

An exact solution is available for this situation using the traditional Navier-Stokes equations. It is given in terms of a two-dimensional stream function, ψ ,

$$\psi = \sin \theta (Ar^3 + Br \ln r + Cr + Dr^{-1}). \quad (36)$$

Here, A , B , C , and D are integration constants that are used to specify boundary conditions. For this case, no-slip is assumed at the cylinder wall and the velocity is assumed to be free-stream at a cylinder some given

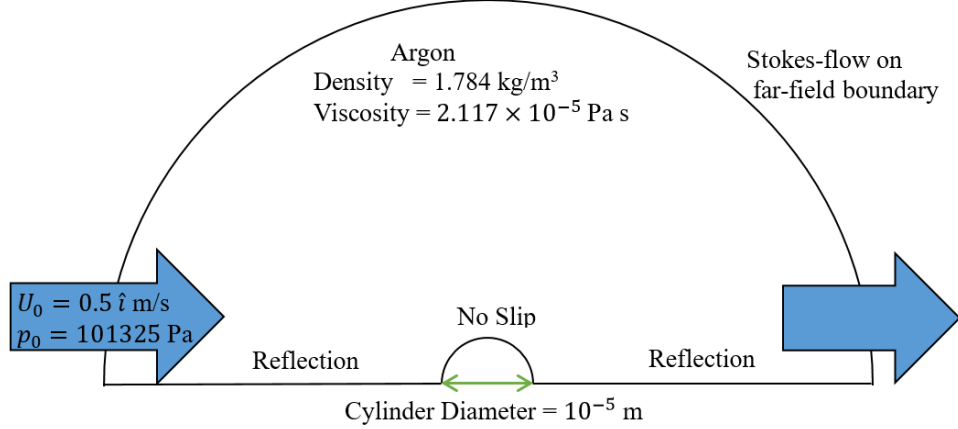


Figure 8: Stokes flow around a circular cylinder.

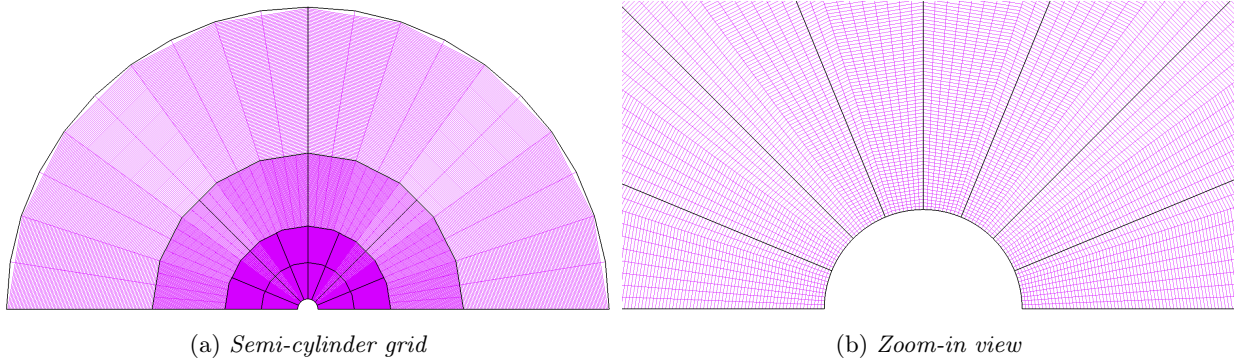


Figure 9: Semi-cylindrical grid used for Stokes-flow calculations. The grid comprises twenty-two blocks at three different refinement levels and 22 880 cells total.

distance from the immersed body. The velocity in polar coordinates can be found as

$$v_\theta = -\frac{\partial \psi}{\partial r}, \quad v_r = \frac{1}{r} \frac{\partial \psi}{\partial \theta}. \quad (37)$$

Once the velocity field is known, the pressure and viscous-stress fields can also be determined by integrating the Navier-Stokes equations. As this problem is symmetric, only half the domain is used for the calculation.

For this computation, a mesh of 22 blocks and 22 880 cell is used, as shown in Figure 9. A zoom-in of the area surrounding the cylinder is shown in Figure 9(b). The boundary condition at the cylinder is no-slip while the symmetry line is modelled as a reflection. On the far-field boundary, the exact solution for Stokes flow is imposed.

Figure 10 compares the DGH moment-closure solutions with the exact solution. The top of each figure is the moment method solution, while the bottom is the reflection of the exact solution. Figure 10(a) compares the prediction for the shear pressure, P_{xy} , with the exact solution. Again, this shear pressure is the negative of the viscous shear stress from the Navier-Stokes equations, τ_{xy} . The breaks in the contour lines are the result of the plotting software being unable to interpolate across block boundaries. One can observe that the two halves are almost identical. The moment method in combination with the DGH scheme is clearly able to predict this classical viscous result. In Figure 10(b), the predicted Mach number and streamlines are compared with the exact result. Once again agreement is very good. The low-speed region in the moment-closure prediction seems to shift downstream slightly, however this may be due to numerical dissipation in this extremely low-speed problem. Finally, the deviation of P_{xx} from the thermodynamic pressure p is shown in Figure 10(c). This value corresponds to the negative of the normal component of the viscous stress in

the traditional Navier-Stokes model. Again agreement is very strong. The moment method seems to over predict the magnitude of the stress in front of the cylinder while slightly under predicting its magnitude behind. Again, this is likely numerical error caused by the extreme low-speed flow leading to a flow problem with very high condition number.

6 Conclusion and Future Work

A new implementation of a coupled space-time discontinuous-Galerkin-Hancock method is presented. This method is designed specifically for the efficient solution of hyperbolic-relaxation equations that result from moment closures of kinetic theory. It may be surprising to some that viscous flow behaviour can be accurately predicted by first-order PDEs. However, the applicability of hyperbolic moment methods to both continuum and non-equilibrium gas flows is now well established. Such a first-order treatment brings many physical and computational advantages to gas flow prediction.

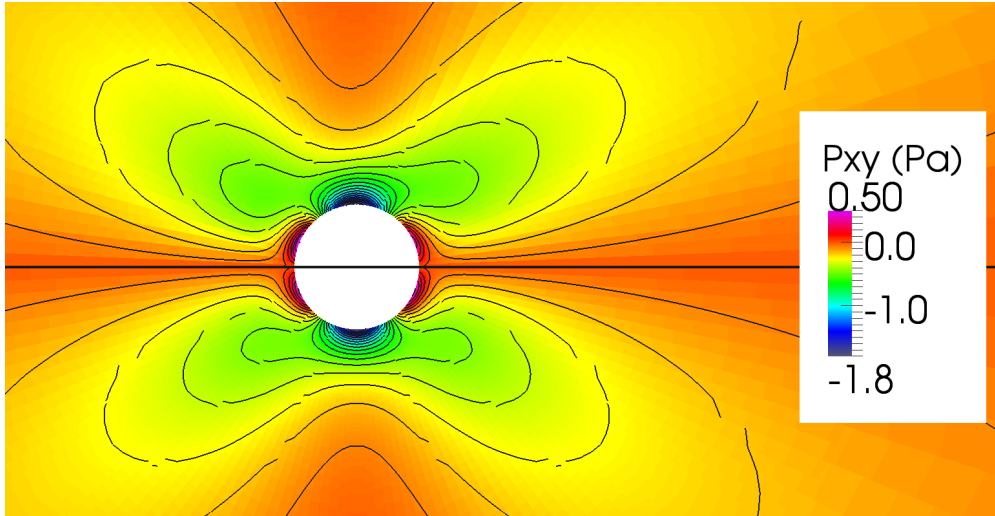
As future work, gains in parallel efficiency for this algorithm on massive computing facilities will be assessed. The application of the scheme to more complex, real-world gas and multiphase flow problems will also be investigated.

7 Acknowledgements

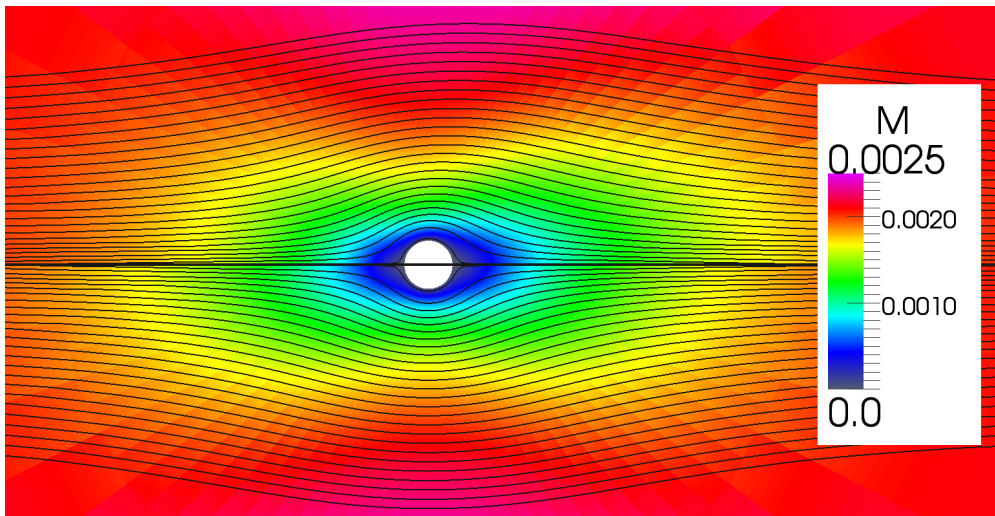
Funding for this research was provided by the Natural Sciences and Engineering Research Council of Canada (NSERC). The authors are very grateful for this support.

References

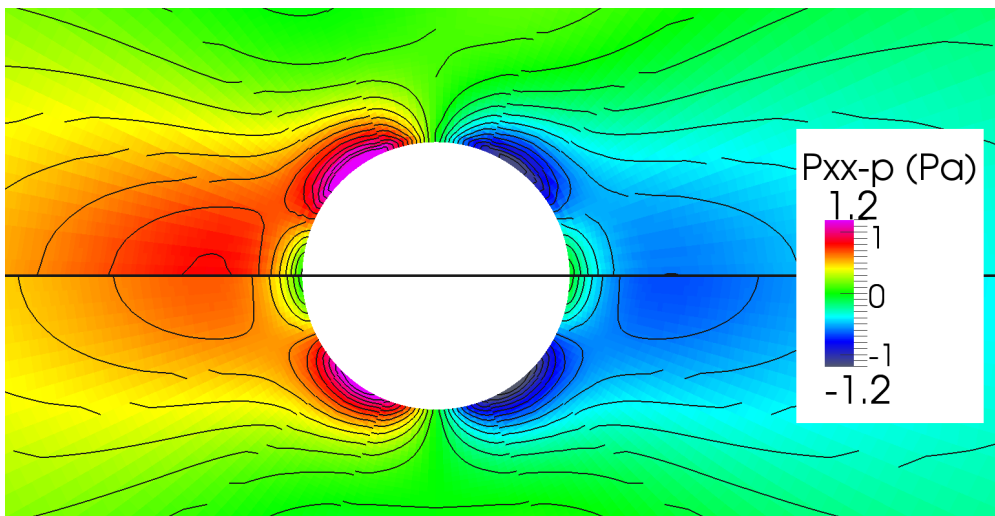
- [1] J. G. McDonald, J. S. Sachdev, and C. P. T. Groth. Application of Gaussian moment closure to micro-scale flows with moving and embedded boundaries. *AIAA J.*, 52:1839–1857, 2014.
- [2] Y. Suzuki and B. van Leer. A discontinuous galerkin method with hancock-type time integration for hyperbolic systems with stiff relaxation source terms. In H. Deconinck and E. Dick, editors, *ICCFD4, Ghent, Belgium, July 10–14, 2006*, pages 59–64, Heidelberg, 2009. Springer-Verlag.
- [3] Y. Suzuki. *Discontinuous Galerkin Methods for Extended Hydrodynamics*. PhD thesis, University of Michigan, 2008.
- [4] G. D. van Albada, B. van Leer, and W. W. Roberts, Jr. A comparative study of computational methods in cosmic gas dynamics. *Astron. Astrophys.*, 108(1):76–84, 1982.
- [5] H. Grad. On the kinetic theory of rarefied gases. *Commun. Pure Appl. Math.*, 2:331–407, 1949.
- [6] W. Dreyer. Maximization of the entropy in non-equilibrium. *Journal of Physics A: Mathematical and General*, 20:6505–6517, 1987.
- [7] I. Müller and T. Ruggeri. *Extended Thermodynamics*. Springer-Verlag, New York, 1993.
- [8] C. D. Levermore. Moment closure hierarchies for kinetic theories. *J. Stat. Phys.*, 83:1021–1065, 1996.
- [9] M. Junk. Domain of definition of Levermore’s five-moment system. *J. Stat. Phys.*, 93(5/6):1143–1167, 1998.
- [10] J. G. McDonald and C. P. T. Groth. Towards realizable hyperbolic moment closures for viscous heat-conducting gas flows based on a maximum-entropy distribution. *Continuum Mech. Thermodyn.*, 25:573–603, 2013.
- [11] J. G. McDonald and M. Torrilhon. Affordable robust moment closures for CFD based on the maximum-entropy hierarchy. *J. Comput. Phys.*, 251:500–523, 2013.
- [12] A. Vié, F. Doisneau, and M. Massot. On the anisotropic Gaussian velocity closure for inertial-particle laden flows. *Commun. Comput. Phys.*, 17(1):1–46, 2015.
- [13] F. Forgues and J. G. McDonald. Higher-order moment models for laminar multiphase flows with accurate particle-stream crossing. *Int. J. Multiphase Flow*, 2018. (submitted).
- [14] A. Harten, P. D. Lax, and B. van Leer. On upstream differencing and Godunov-type schemes for hyperbolic conservation laws. *SIAM Rev.*, 25(1):35–61, 1983.
- [15] B. Einfeldt. On Godunov-type methods for gas dynamics. *SIAM J. Numer. Anal.*, 25:294–318, 1988.



(a) Shear pressure, P_{xy}



(b) Mach number and streamlines



(c) Deviatoric x-direction pressure, $P_{xx} - p$

Figure 10: Stokes flow around a circular cylinder. Top half is the ten-moment solution while the bottom half is the reflection of the exact Navier-Stokes solution.

- [16] J. S. Sachdev, C. P. T. Groth, and J. J. Gottlieb. A parallel solution-adaptive scheme for predicting multi-phase core flows in solid propellant rocket motors. *Int. J. Comput. Fluid Dyn.*, 19(2):159–177, 2005.
- [17] X. Gao and C. P. T. Groth. A parallel adaptive mesh refinement algorithm for predicting turbulent non-premixed combusting flows. *Int. J. Comput. Fluid Dyn.*, 20(5):349–357, 2006.
- [18] V. Venkatakrishnan. On the accuracy of limiters and convergence to steady state solutions. Paper 93-0880, AIAA, January 1993.
- [19] P. L. Bhatnagar, E. P. Gross, and M. Krook. A model for collision processes in gases. I. small amplitude processes in charged and neutral one-component systems. *Physical Rev.*, 94(3):511–525, 1954.